An Experimental and Numerical Study of Roughness-Induced Instabilities in a Mach 3.5 Boundary Layer

Michael Kegerise, Rudolph King, Lewis Owens,
Meelan Choudhari, Andrew Norris, Fei Li, and Chau-Lyan Chang
NASA Langley Research Center
1A East Reid Street, MS 170
Hampton, VA 23681
United States

michael.a.kegerise@nasa.gov

ABSTRACT

Progress on a joint experimental and numerical study of laminar-to-turbulent transition induced by an isolated roughness element in a high-speed laminar boundary layer is reported in this paper. The numerical analysis suggests that transition is driven by the instability of high- and low-speed streaks embedded in the wake of the isolated roughness element. In addition, spatial stability analysis revealed that the wake flow supports multiple modes (even and odd) of convective instabilities that experience strong enough growth to cause transition. The experimental measurements, which included hot-wire and pitot-probe surveys, confirmed the existence of embedded high- and low-speed streaks in the roughness wake. Furthermore, the measurements indicate the presence of both even and odd modes of instability, although their relative magnitude depends on the specifics of the roughness geometry and flow conditions (e.g., the value of Re_{kk} or k/δ). For the two test cases considered in the measurements (Re_{kk} values of 462 and 319), the even mode and the odd mode were respectively dominant and appear to play a primary role in the transition process.

1.0 INTRODUCTION

On many hypersonic vehicles, laminar-to-turbulent transition is dominated by surface roughness. That roughness can be either distributed, such as the thermal protection system tiles on the Space Shuttle Orbiter, or it can be isolated, in the form of protruding gap fillers or tile-damage cavities on the Orbiter. In the case of reentry vehicles, isolated roughness is of particular concern because it can cause transition at a Mach number much higher than expected, leading to high local heating levels and asymmetric aerodynamic loads on the vehicle [1]. Alternatively, for hypersonic air-breathing propulsion systems, turbulent flow at the scramjet inlet is desired to mitigate engine unstart [2]. To ensure a turbulent flow in that case, a spanwise periodic array of roughness elements on the vehicle forebody can be used to force laminar-to-turbulent transition. In either case, accurate prediction tools for roughness-induced transition are critical to vehicle design, performance, and safety.

The state-of-the-art approach for prediction of isolated roughness-induced transition is to utilize engineering correlations based on a critical roughness Reynolds number such as Re_{kk} [3]. While this approach can be effective, there are several limitations. In particular, correlations are applicable only to the geometry for which they were developed, they often exhibit large data scatter which produces large uncertainty in the predicted transition location, and they offer no physical insight to the instability and transition mechanisms. An alternative approach, one which should afford greater accuracy in our transition predictions, is to develop prediction methodologies that are based on the underlying physical mechanisms associated with isolated roughness-induced transition. To that end, we must first determine how an isolated roughness causes transition in a

high-speed boundary layer. Recent computations by Choudhari *et al.* [4] suggest that transition due to an isolated roughness element is driven by the instability of high- and low-speed streaks embedded in the wake of the roughness element. More specifically, the wake flow was found to support multiple modes of convective instabilities that experience strong enough growth to cause transition. To verify the existence of the embedded streaks and their instability modes, we require off-body mean and dynamic flow-field measurements in the downstream wake of the roughness element. If streak instabilities prove to be the primary mechanism for transition in this case, then one possible approach for transition prediction would be to develop an N-factor method based on the growth of streak instabilities.

In this paper, we present our progress on a joint experimental and numerical study of laminar-to-turbulent transition produced by an isolated roughness element in a high-speed laminar boundary layer. The test geometry for this study is a flat plate with a sharp leading edge and a freestream Mach number of 3.5. This supersonic edge Mach number is relevant to a number of hypersonic applications (*e.g.*, reentry bodies) where the boundary layer edge Mach number can be supersonic. Since the physics of roughness-induced transition is primarily governed by the local flow conditions, investigating roughness effects at supersonic edge Mach numbers will, in a broader context, lead to a more complete understanding of the hypersonic roughness-induced transition problem. For the experimental portion of this study, the focus is on detailed off-body flow-field measurements in the downstream wake of an isolated roughness element attached to the flat plate. Although the scope of our study includes measurements and computations for a range of roughness heights and planform shapes, this paper will focus on results for a single roughness of moderate height (k/δ of about one half) and a diamond planform shape. To minimize the influence of freestream disturbances on our measurements, the experiment was conducted in the NASA Langley Supersonic Low-Disturbance Tunnel (SLDT), which is a quiet wind tunnel facility with root-mean-square (RMS) static pressure fluctuations that are less than 0.05% of the mean static pressure. For the computational portion of this study, the laminar base flow in the presence of the roughness element was computed using a Navier-Stokes solver. Spatial instability analysis of the streamwise elongated wake behind the roughness element was then applied. Because of the inhomogeneous nature of the wake in both the wall-normal and spanwise directions, a planar, partial-differential eigenvalue problem was solved to predict the instability characteristics within the wake. Multiple families of unstable modes are known to exist at each streamwise station and the amplification rates of each relevant family of modes were integrated in the streamwise direction to determine the modes that are likely to dominate the instability growth within the wake.

2.0 EXPERIMENTAL SETUP

The experimental measurements were performed in the Supersonic Low-Disturbance Tunnel (SLDT) at NASA Langley Research Center. This "quiet" wind tunnel facility produces a Mach 3.5 freestream with RMS static pressure fluctuations that are less than 0.05% of the mean static pressure. Since boundary-layer transition is known to be sensitive to the disturbance environment, testing in a low-noise facility, such as the SLDT, is necessary to simulate transition in the low-disturbance environment encountered during high-altitude flight. Details on the facility operation and performance characteristics are provided in Beckwith *et al.* [5] and Chen [6]. For the current experiment, the facility was configured with a Mach 3.5 two-dimensional rapid-expansion nozzle and typical nozzle performance characteristics are shown in Fig. 1. Here, the fluctuating pitot pressure RMS (in a frequency band from 100 Hz to 100 kHz) and the Mach number variation along the nozzle centerline are shown for different freestream unit Reynolds numbers. The abscissa in both plots denotes the distance from the nozzle throat, and the nozzle exit is at 39.4 cm. Generally, the uniform quiet-flow core of the nozzle begins at the point where the freestream reaches the design Mach number of 3.5 and ends at the point where the freestream disturbance levels reach 0.05%. Therefore, at the nominal test unit Reynolds number of 10×10^6 m^{-1}, the

uniform quiet-flow core is seen to start at 14 cm and to end at approximately 35 cm.

A CAD model of the flat plate, support hardware (model sting and strut), and model traverse mechanism is shown in Fig. 2. The flat plate was machined from 15-5 stainless steel and is 406.4 mm long, 228.6 mm wide at the leading edge, and tapers to 76.2 mm wide at the trailing edge. The leading edge has a 15° bevel on the bottom side of the plate and a nominal leading-edge thickness of 0.05 mm. The trapezoidal shape of the flat plate was designed to alleviate side wall blockage effects that were identified in earlier testing with a rectangular flat plate model. The top surface of the flat plate was polished to a roughness level of 0.0254 μm RMS and had no visable scratches at 3 times magnification. The flat plate was instrumented with 15 type-K thermocouples, positioned along the model centerline, for measurement of the surface temperature. When installed in the SLDT, the leading edge of the model was positioned on the nozzle centerline, 14 cm downstream from the nozzle throat. At that position, and a nominal test unit Reynolds number of 10×10^6 m^{-1}, quiet flow with a constant Mach number of 3.5 extends over the first 21 cm of the model. To survey the boundary layer on the flat-plate model, a sting-mounted, 3-axis traverse mechanism was utilized, and details on the design and calibration of the traverse mechanism can be found in Kegerise *et al.* [7].

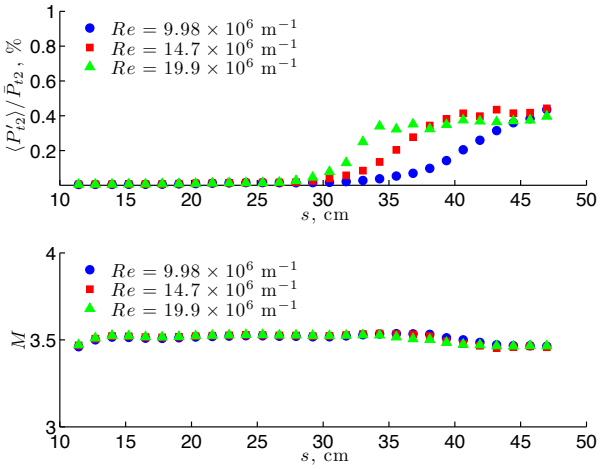

Figure 1: Fluctuating pitot pressure RMS (in a frequency band from 100 Hz to 100 kHz) and Mach number variation along the nozzle centerline for different freestream unit Reynolds numbers.

Figure 2: CAD model of the flat plate, support hardware (model sting and strut), and model traverse mechanism.

Boundary layer surveys were performed with two different probe types. The first probe was a miniature pitot probe, with the end flattened to a height of 101.6 μm, that was used to measure mean Mach number profiles. The second probe was a miniature hot-wire probe that was used to measure mean and fluctuating mass-flux profiles. The hot-wire probe was operated in a constant-temperature (CTA) mode at a high overheat ratio where the output is primarily sensitive to mass-flux fluctuations, and total-temperature fluctuations can be neglected [8]. The hot-wire sensors were platinum-plated tungsten, with a 3.8 μm diameter and a 0.5 mm nominal length (length-to-diameter ratio of 132), welded to the ends of the hot-wire prongs. The frequency response of the hot-wire, which was optimized via square-wave injection, was typically 270 kHz. The hot-wire probe was also operated in a cold-wire mode to measure mean total temperature profiles. The primary use of that data was to correct the hot-wire data for changes in the mean total temperature across the boundary layer. Further details on the design, calibration, and positioning of the boundary-layer probes, as well as procedures for collecting and processing the data, can be found in Kegerise [7].

The isolated roughness elements used in our experimental study were fabricated with a low compressibility

polyester shim stock material that is available in a range of heights ($k = 76.2$ μm to 635 μm) and is easily cut into arbitrary planforms via laser ablation. The roughness elements were then attached to the model surface with cyanoacrylate adhesive. In this paper, however, the focus is on a single roughness element that has a diamond-shaped planform with equal edge lengths of 2.54 mm. The height of the roughness element, which was measured *in situ* with a digital microscope system, was 345.4 ± 7 μm. The center of roughness element was positioned on the model centerline, 41.5 mm from the leading edge.

3.0 NUMERICAL METHODS

To obtain the mean-flow solution in the presence of the roughness element, the compressible Navier-Stokes equations were solved using local time stepping in conjunction with an implicit technique. The piecewise parabolic method was used to extend the first-order low diffusion flux splitting scheme (LDFSS) to 4th order for advection terms in smooth regions of the flow. The immersed boundary (IB) technique, as implemented by Choi *et al.* [9] and Ghosh, *et al.* [10], was used to simulate the effects of the roughness element on the surrounding flow. For simplicity, the inflow conditions were defined via the self-similar solution to the boundary-layer equations at the freestream conditions of interest. The computations were limited to a narrow spanwise region centered on the roughness element, and any large-scale three-dimensional effects associated with the finite span of the model were neglected. The number of grid points in the streamwise, wall-normal, and spanwise directions were 1281, 289, and 45, respectively, so the total number of cells within the 3-D immersed boundary mesh over one half of the spanwise region was approximately 16 million. The grid count, as well as the relative grid distribution, was based on previous computations for a spanwise periodic array of roughness elements, which has a flow field that is very similar to that for the isolated roughness element [11]. Typically, the mean flow computations were continued for at least 10000 iterations after the residual stagnated around $O(10^{-12})$, to ensure that any locally separated regions were no longer evolving.

The spatial stability of the computed roughness wake was examined at several streamwise stations using the methodology described in Li and Choudhari [12]. Since the spanwise and wall-normal length scales of the flow in the roughness wake are comparable to each other, the modified boundary-layer flow has a strongly inhomogeneous character in both the z and y directions. Therefore, the stability characteristics were studied by solving a planar, partial-differential eigenvalue problem to predict the instability characteristics in the wake. In this analysis both even (symmetric or varicose) and odd (antisymmetric or sinuous) modes of instability were examined.

4.0 RESULTS

4.1 Baseline Laminar Boundary Layer

To characterize the base flow and to establish the inflow conditions for the computations, surveys of the laminar boundary layer on the flat plate model were performed with pitot and hot-wire probes. Several streamwise stations along the model centerline were considered, starting at $x = 41.5$ mm and ending at $x = 191.5$ mm. For a subset of these stations, boundary layer surveys at several spanwise locations, ranging from $z = -10$ mm to $z = 10$ mm, were performed to assess the two-dimensionality of the baseline boundary layer. A sample of the centerline boundary layer data is shown in Fig. 3 for two streamwise stations and two freestream unit Reynolds numbers. All data were acquired at a freestream total temperature of 319.3 K and the measured wall temperature was 290 K. The ordinate for each plot is the similarity variable $\eta = y\sqrt{Re_x}/x$, and the total temperature, mass-flux, and velocity profiles were normalized by their respective edge values. The similarity

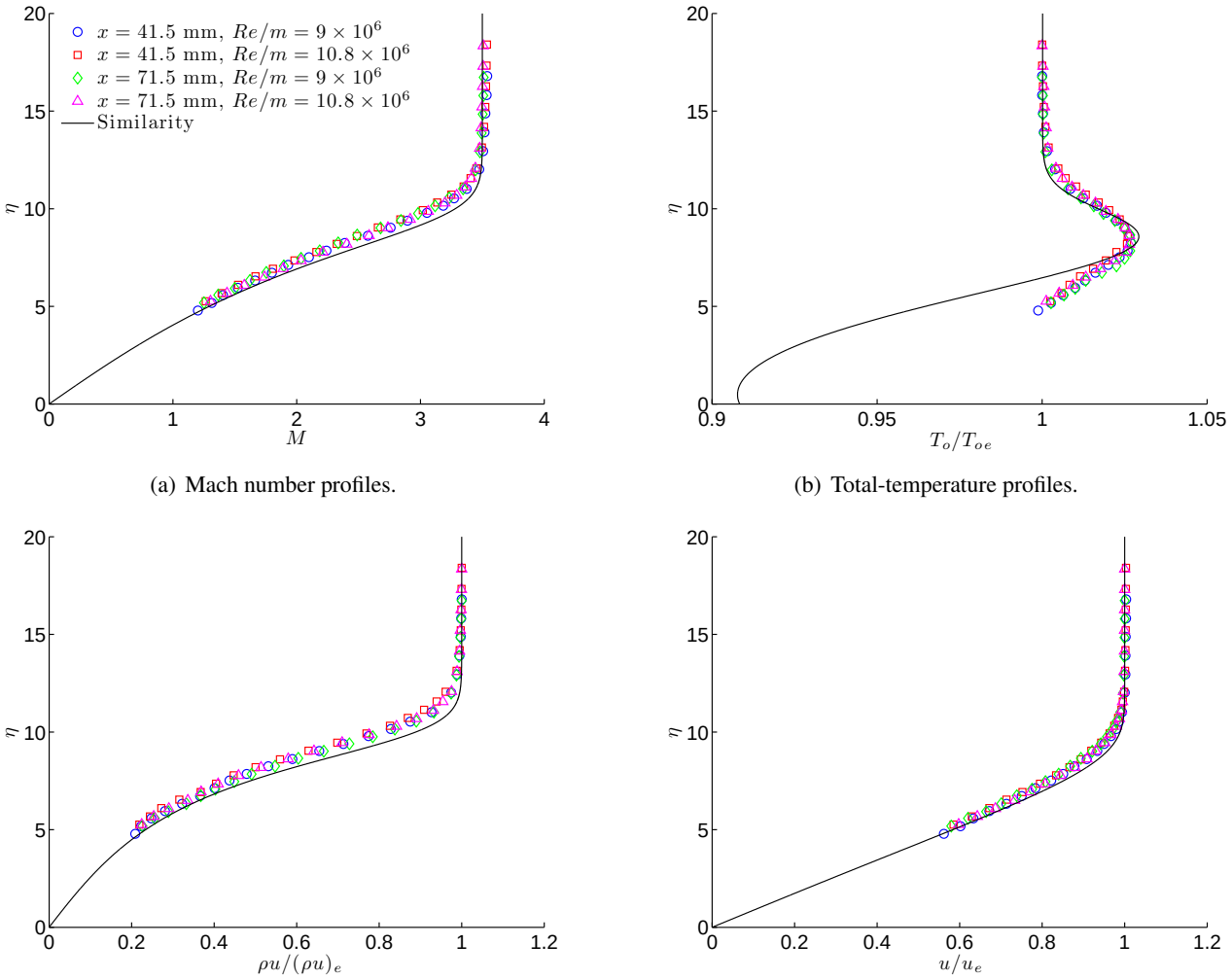

(a) Mach number profiles.

(b) Total-temperature profiles.

(c) Mass-flux profiles.

(d) Streamwise velocity profiles.

Figure 3: Baseline laminar boundary layer profiles along the model centerline. All data were acquired at a freestream total temperature of 319.3 K. The similarity solution was computed for a constant wall temperature of 290 K.

solution for a Mach 3.5 sharp leading edge flat plate with a constant wall temperature of 290 K is included in the plots for comparison. An inspection of the measured boundary layer profiles at different spanwise locations (not shown here for brevity) indicates that the flow is essentially two dimensional over the survey region.

The collapse of the measured boundary layer profiles with the similarity scaling suggests that the laminar base flow is self similar. When compared to the theoretical similarity solution, however, the measured profiles were found to be slightly thicker. In part, this discrepancy is due to a weak adverse pressure gradient that exists over the measurement region. An additional reason for this discrepancy may be that the similarity solution is based on a sharp leading edge of vanishing thickness, while the actual model leading edge has a small but finite thickness. Measurements of the leading-edge geometry are forthcoming, and computations with that geometry and the measured boundary layer edge conditions may yield better agreement. Nevertheless, our first step was to use the similarity solution as the inflow condition for computations with the roughness element.

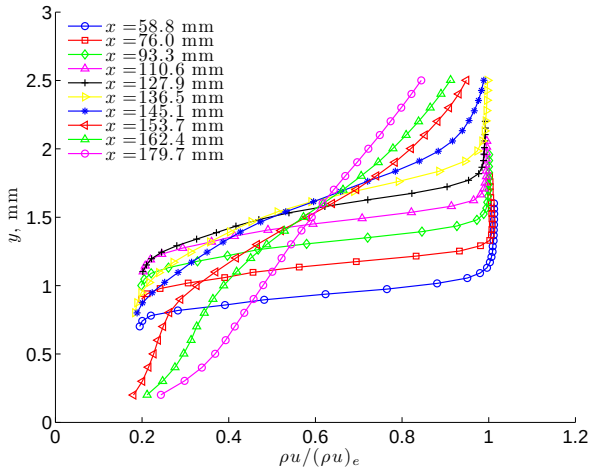

(a) Mean mass-flux profiles along centerline of roughness wake.

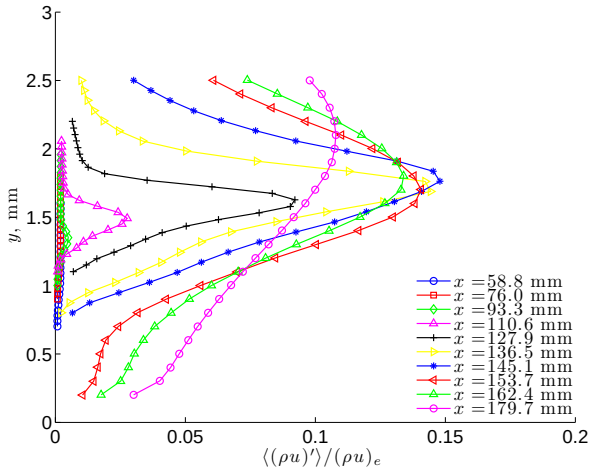

(b) RMS mass-flux profiles (over a 30 kHz to 200 kHz frequency band) along centerline of roughness wake.

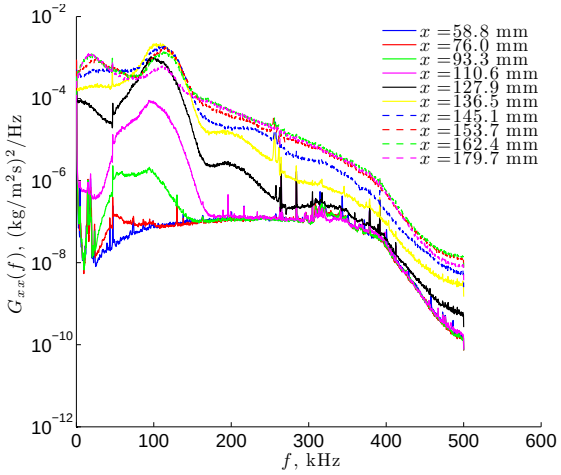

(c) Centerline mass flux power spectral densities at the peak of the RMS mass-flux profile for different streamwise stations.

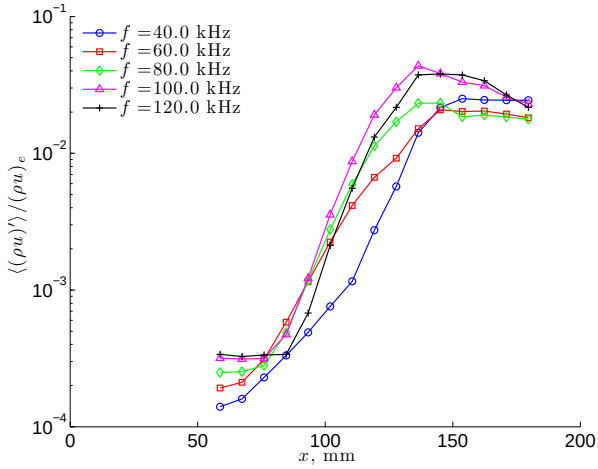

(d) Streamwise evolution of peak RMS mass flux at different frequencies.

Figure 4: Mass-flux data along the centerline of the roughness element wake. Here, the nominal freestream conditions were $\mathbf{P_o = 206.8}$ kPa, $\mathbf{T_o = 319.3}$ K, and $\mathbf{Re = 10.8 \times 10^6}$ m^{-1}. The roughness element was $\mathbf{k = 345.4}$ μm tall and located 41.5 mm from the leading edge. For these conditions, the nominal roughness Reynolds number was $\mathbf{Re_{kk} = 462}$.

4.2 Isolated Roughness Results

To obtain an overall picture of the transition process in the wake of the isolated roughness element, we first made boundary layer surveys along the wake centerline. These surveys were performed at a freestream unit Reynolds number of 10.8×10^6 m^{-1} and a nominal total temperature of 319.3 K. For these freestream conditions, the roughness Reynolds number, Re_{kk}, which is based on undisturbed conditions at the height of the roughness, was 462, and the ratio of the roughness height to boundary layer thickness was $k/\delta = 0.48$. The conditions for this roughness case were sufficient to bring about the beginning stages of breakdown to turbulence within the measurement region, which extended to 138.2 mm ($x = 179.7$ mm) downstream of the roughness element. Our current numerical simulation results are for a roughness with the same planform geometry but a different height

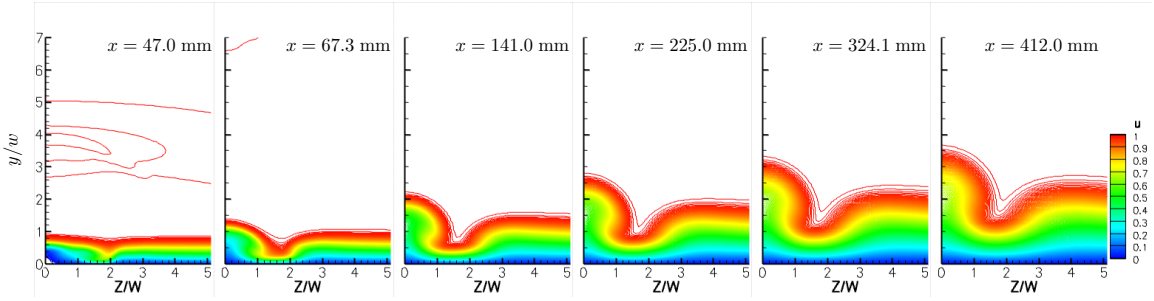

Figure 5: Computed mean streamwise velocity contours in the roughness wake. Due to the spanwise symmetry of the flow field, only the right half is shown. Both abscissa and ordinate are normalized by the frontal half width of the roughness element.

of 381 μm, which provides an $Re_{kk} = 547$ and $k/\delta = 0.55$ for the freestream conditions that were considered. Therefore, when we make comparisons between the experimental measurements and the computational results in this section, they will be qualitative in nature.

Mass-flux data along the centerline of the roughness element wake are shown in Fig. 4. In Fig. 4a, the mean mass-flux profiles for several streamwise stations are presented. Near the roughness element, the mean flow is characterized by a lofted shear layer region, lying a few roughness heights away from the wall, that moves outward with increasing streamwise distance. Here, the boundary layer is substantially thicker than the baseline laminar boundary layer. By $x = 136.5$ mm, we observe an increased wall-normal spreading of the shear layer region that signals the beginning stages of breakdown to turbulence. With further distance downstream, the mean mass-flux profiles become fuller and more indicative of a turbulent boundary layer. The overall character of the measured mass-flux profiles within the laminar region is consistent with the computations. Contour plots of the computed mean streamwise velocity in the y-z plane are shown in Fig. 5. Here, we see a strong upwelling of the boundary layer, presumably associated with the horseshoe vortex system that begins near the front of the roughness element, that gives rise to the lofted shear layer profiles. The computations also display the outward movement of the shear layer and the persistence of this structure for large distances downstream of the roughness element.

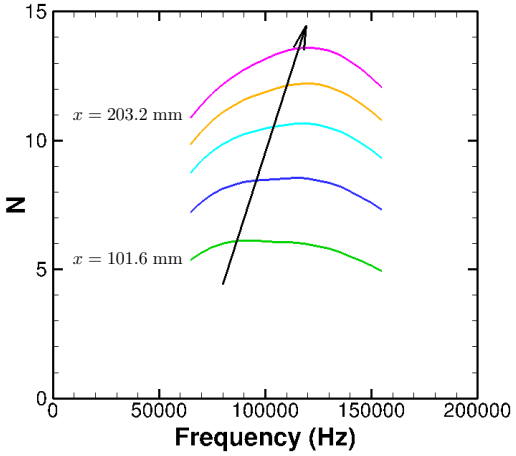

Figure 6: Computed N-factor spectra for the even mode of instability at several streamwise stations.

The lofted shear layer character of the mean centerline profiles sets the stage for an inviscid type of instability. Evidence of that instability is provided by the broadband RMS mass-flux profiles (over a frequency band from 30 kHz to 200 kHz) that are shown in Fig. 4b. Initially, the mass-flux fluctuations associated with the instability are below the noise floor of the hot-wire anemometer and we don't see any increase until $x = 93.3$ mm. From that point on, the mass-flux fluctuations display substantial growth in the streamwise direction, and have peak levels in the lofted shear layer region of the mean flow. The mass-flux fluctuations saturate at $x = 145.1$ mm and then decay and spread throughout the boundary layer as the breakdown to turbulent flow begins.

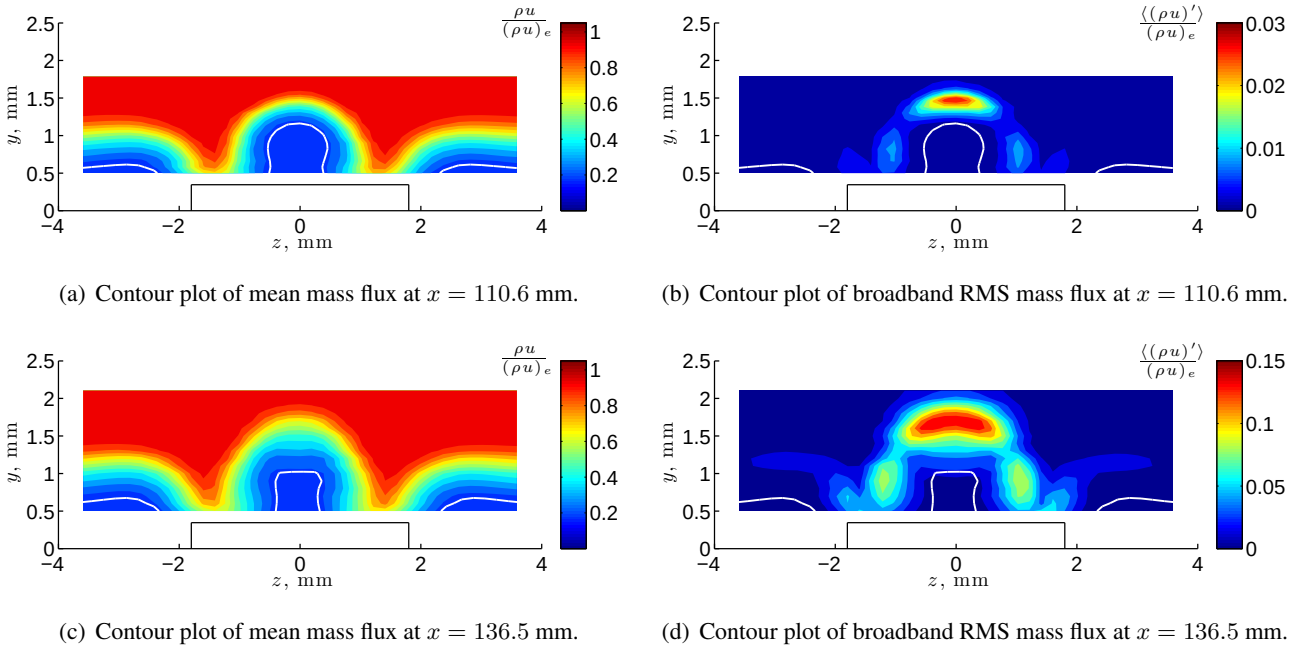

(a) Contour plot of mean mass flux at $x = 110.6$ mm.

(b) Contour plot of broadband RMS mass flux at $x = 110.6$ mm.

(c) Contour plot of mean mass flux at $x = 136.5$ mm.

(d) Contour plot of broadband RMS mass flux at $x = 136.5$ mm.

Figure 7: Planar survey of the roughness element wake at two different streamwise stations. The black line at the bottom center of each plot represents the projected outline of the roughness element and the white line in each plot is a Mach 1.2 contour line. The nominal freestream conditions were $\mathbf{P_o = 206.8}$ kPa, $\mathbf{T_o = 319.3}$ K, and $\mathbf{Re = 10.8 \times 10^6}$ m^{-1}.

To identify the frequencies associated with the instability in the roughness wake, the fluctuating mass-flux time series were processed to obtain power spectral densities (PSD) and sample results are presented in Fig. 4c. Here, the mass-flux PSD at the peak of the RMS mass-flux profile for different streamwise stations is shown. The power spectral densities reveal an unstable band of frequencies, centered around 100 kHz, that grows rapidly with streamwise position and saturates by $x = 145.1$ mm. As we progress further downstream, this spectral band decays somewhat and the mass-flux PSD become more broadband as the flow transitions to turbulence. We also observe a shift in the unstable band of frequencies towards higher values with increasing streamwise position. That trend is predicted by the spatial stability analysis and an example is shown in Fig. 6, where the computed linear amplification (N-factor) spectra for the even mode of instability are presented. The stability analysis also predicts peak unstable frequencies that are comparable to the measurements.

An alternative view of the spectral data is presented in Fig. 4d, where the streamwise evolution of the peak RMS mass flux is plotted for selected frequencies (for a given frequency, the RMS was derived from the mass-flux PSD by integrating over a ± 2 kHz frequency band). Generally, frequencies around 100 kHz have the largest growth rates and they experience the most overall growth over the measurement region.

To obtain a more complete picture of the roughness wake and the associated instabilities, detailed hot-wire surveys in the y-z plane at two streamwise stations were performed. The first station was located at $x = 110.6$ mm, where the instability growth appears to be linear. The second station was at $x = 136.5$ mm, where the mass-flux disturbances saturate and the mean flow begins to show increased wall-normal spreading; *i.e.*, at the beginning of breakdown to turbulence. At each station, data were collected in spanwise increments of $\Delta z = 0.2$ mm and confined to a region between $z = \pm 3.6$ mm. In the wall-normal direction, approximately 18 heights were considered in increments of $\Delta y = 0.08$ mm or 0.10 mm. Color contour plots of the mean mass-flux and the broadband RMS mass-flux for the two streamwise stations are shown in Fig. 7. The white

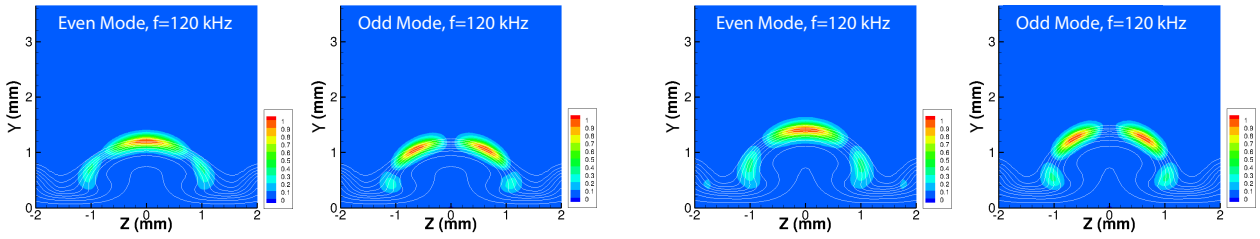

(a) $x = 71.1$ mm. (b) $x = 91.4$ mm.

Figure 8: Computed representative mass flux mode shapes for the even and odd modes of instability at two streamwise locations. The white lines are contours of the mean mass-flux distribution.

line in each plot is a Mach 1.2 contour line that was obtained from planar surveys with the pitot probe. Hot-wire data below this line should be viewed with caution because transonic effects on the hot-wire response are not accounted for in the hot-wire calibration. In comparison to the computed mean velocity contours shown in Fig. 5, the measured flow field in the roughness wake is quite similar. In particular, we observe the strong upwelling in the roughness wake that causes a substantial thickening of the boundary layer in comparison to the baseline flow. The wake centerline is characterized by a region of relatively low-speed fluid that persists for a large downstream distance. That feature is indicative of a low-speed streak extending downstream of the roughness. On either side of this low-speed streak, and just inboard of the roughness element edges (located at $z = \pm 1.8$ mm), the boundary layer becomes very thin relative to the baseline laminar boundary layer—a feature that is indicative of a pair of high-speed streaks extending downstream of the roughness. The presence of these embedded high- and low-speed streaks, and the correspondingly strong spanwise and wall-normal shear, sets the stage for an instability growth in the roughness wake. In view of the broadband RMS mass-flux contours presented in Figs. 7b and 7d, we see that the mass-flux fluctuations in the roughness wake are concentrated in regions of high spanwise and wall-normal shear. However, the maximum RMS mass flux for the present roughness case lies along the wake centerline in the shear layer region above the low-speed streak.

The spatial stability analysis of the roughness wake predicts two families of instability modes, herein called the even and odd modes, respectively. Figure 8 presents representative mass-flux mode shapes for the even and odd modes of instability at two streamwise locations. Choudhari *et al.* [4] have previously shown that the even mode initially grows more rapidly than the odd mode in the case of roughness heights around $k/\delta \approx 0.5$. We may therefore expect the even mode to dominate the transition process in the wake of the current roughness case. In an attempt to identify these instability modes, and to potentially determine which one is likely responsible for transition, we extracted spatial distributions of RMS mass-flux fluctuations at selected frequencies from the planar survey data. To that end, at each point in the plane survey, the mass-flux PSD was calculated and the RMS mass-flux at a given frequency was obtained by integrating the PSD over a ± 2 kHz frequency band about the frequency of interest. The results are presented as color contour plots in Fig. 9 for both streamwise stations and for a range of frequencies. In general, and similar to the broadband fluctuations, the mass-flux fluctuations for each frequency are concentrated in regions of high spanwise and wall-normal shear, and the peak mass-flux fluctuations lie along the wake centerline in the shear layer region above the low speed streak. The most dominant frequency is at 100 kHz, which is consistent with the centerline measurements presented earlier. For frequencies of 80 kHz and above, the spatial distributions for the mass-flux fluctuations are very similar to the even mode of instability. At 60 kHz, however, the spatial distribution appears to have elements of both instability modes, particularly for the most downstream station. This is certainly possible given that the odd mode generally has its peak amplification at frequencies lower than the most amplified even

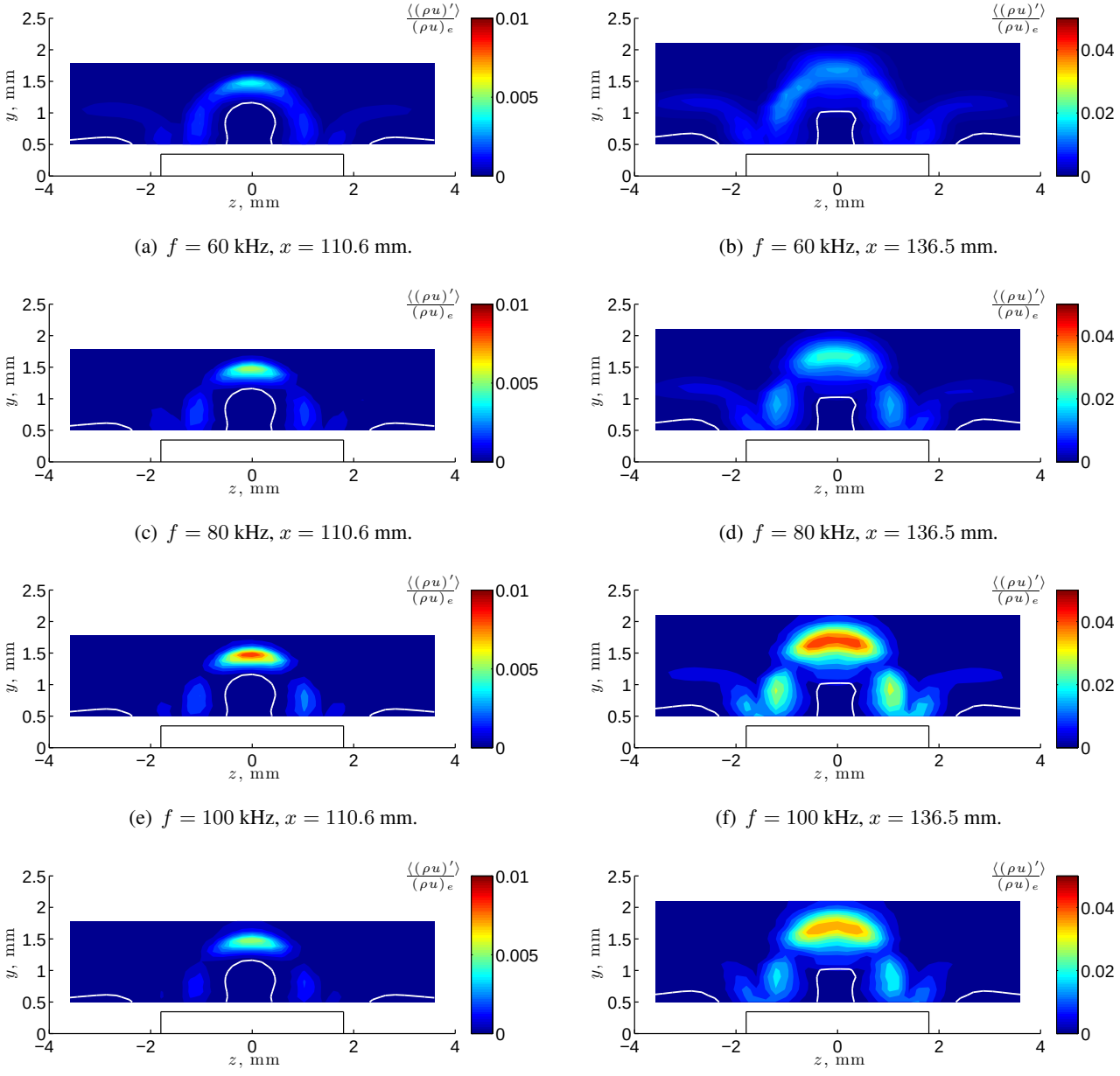

(a) $f = 60$ kHz, $x = 110.6$ mm.

(b) $f = 60$ kHz, $x = 136.5$ mm.

(c) $f = 80$ kHz, $x = 110.6$ mm.

(d) $f = 80$ kHz, $x = 136.5$ mm.

(e) $f = 100$ kHz, $x = 110.6$ mm.

(f) $f = 100$ kHz, $x = 136.5$ mm.

(g) $f = 120$ kHz, $x = 110.6$ mm.

(h) $f = 120$ kHz, $x = 136.5$ mm.

Figure 9: Contour plots of the RMS mass flux at selected frequencies and for different streamwise stations. The black line at the bottom center of each plot represents the projected outline of the roughness element and the white line in each plot is a Mach 1.2 contour line. The nominal freestream conditions were $\mathbf{P_o = 206.8}$ kPa, $\mathbf{T_o = 319.3}$ K, and $\mathbf{Re = 10.8 \times 10^6\ m^{-1}}$.

mode, and both modes are amplified over a broad range of frequencies. Unfortunately, with our single point measurement technique, we cannot produce an independent measurement of each mode. Nevertheless, as we move downstream toward breakdown, the bulk of the fluctuating energy has a spatial distribution similar to the even mode, and for the present roughness case, that mode appears to be responsible for transition.

Measurements in the roughness wake were also performed at a lower Reynolds number of 9.0×10^6 m^{-1},

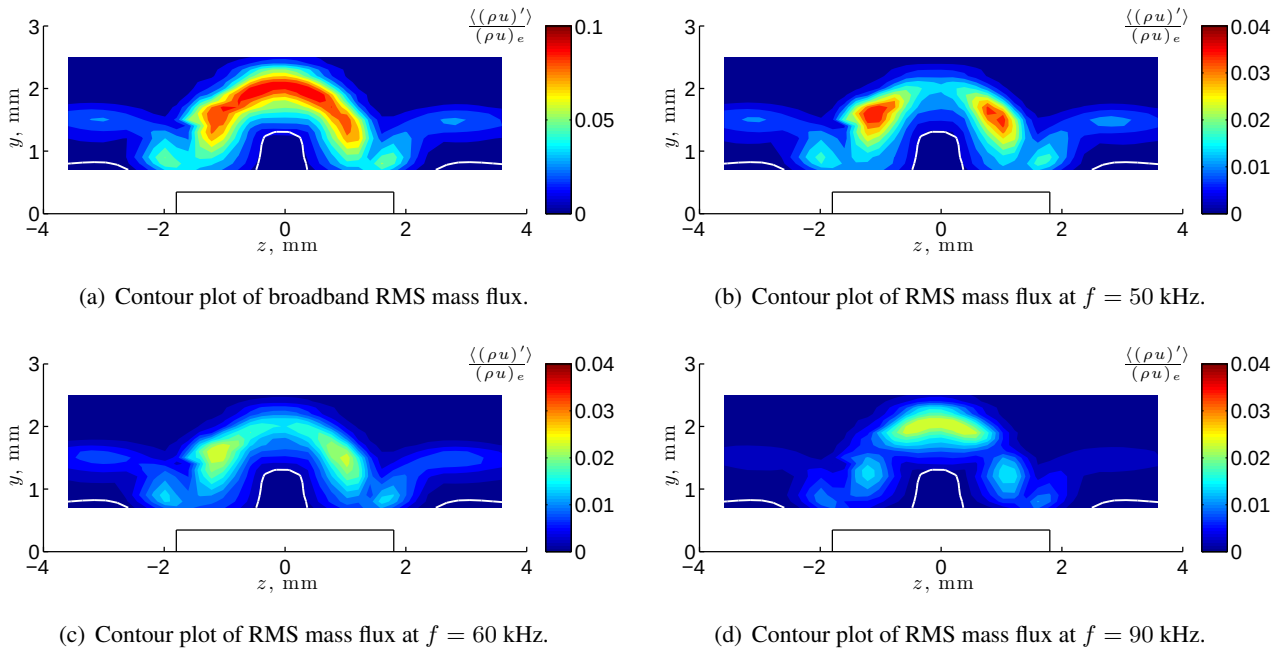

(a) Contour plot of broadband RMS mass flux.

(b) Contour plot of RMS mass flux at $f = 50$ kHz.

(c) Contour plot of RMS mass flux at $f = 60$ kHz.

(d) Contour plot of RMS mass flux at $f = 90$ kHz.

Figure 10: Planar survey of the roughness element wake at $\mathbf{x = 188.3}$ mm. The black line at the bottom center of each plot represents the projected outline of the roughness element and the white line in each plot is a Mach 1.2 contour line. The nominal freestream conditions were $\mathbf{P_o = 172.4}$ kPa, $\mathbf{T_o = 319.3}$ K, and $\mathbf{Re = 9.0 \times 10^6}$ $\mathbf{m^{-1}}$.

where $Re_{kk} = 319$ and $k/\delta = 0.44$. Sample results are shown in Fig. 10 where contour plots of the mass-flux fluctuations for the broadband case and for selected frequencies are plotted for a streamwise station of $x = 188.3$ mm. Although not show here, the mean mass flux contours were very similar to the previous case; *i.e.*, the mean flow in the roughness wake has embedded high- and low-speed streaks. In contrast to the higher Reynolds number case, the broadband fluctuations are distributed more widely in the spanwise direction. Upon examining the fluctuations at different frequencies, we see that this occurs because both even and odd modes of instability are present in the roughness wake at this streamwise location. The spatial distribution of the mass-flux fluctuations at 50 kHz is similar in shape to the odd mode instability (see Fig. 8), while for higher frequencies, the spatial distribution is similar in shape to the even mode instability. However, the odd mode is dominant for this case and it is expected to play a more prominent role in the transition process. This trend, in which the odd mode becomes dominant with decreasing roughness Reynolds number is consistent with previous spatial stability calculations [4].

4.3 Recent Progress on the Numerical Simulations and Mean-Flow Comparisons

In the previous section, comparisons between the experimental measurements and the computational results were qualitative in nature due to the differing roughness geometry and in-flow conditions. Recently, we have computed the laminar flow around and downstream of a roughness element using the flow conditions and geometry of the experimental measurements ($Re = 10.8 \times 10^6$ m^{-1} and $Re_{kk} = 462$). These computations were performed on a body-fitted grid with the VULCAN (Viscous Upwind Algorithm for Complex Flow Analysis) code, which is a Navier-Stokes flow solver for structured, cell-centered, multi-block grids [13]. The stability analysis of the newly computed mean flow is still underway and so comparisons between the computations and experimental results in this section will be focused on the mean flow.

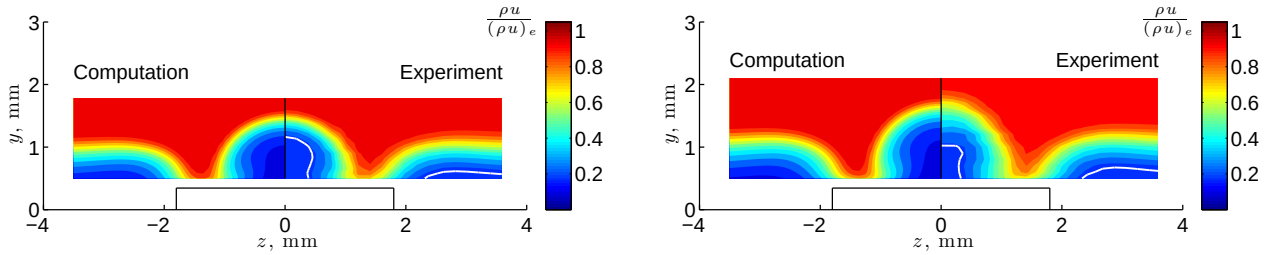

(a) Contour plot of mean mass flux at $x = 110.6$ mm.

(b) Contour plot of mean mass flux at $x = 136.5$ mm.

Figure 11: Comparison of the measured and computed mean mass-flux contours in the y-z plane at two different streamwise stations. The black line at the bottom center of each plot represents the projected outline of the roughness element and the white line in each plot is a Mach 1.2 contour line. The nominal freestream conditions were $\mathbf{P_o} = 206.8$ kPa, $\mathbf{T_o} = 319.3$ K, and $\mathbf{Re} = 10.8 \times 10^6$ m^{-1}.

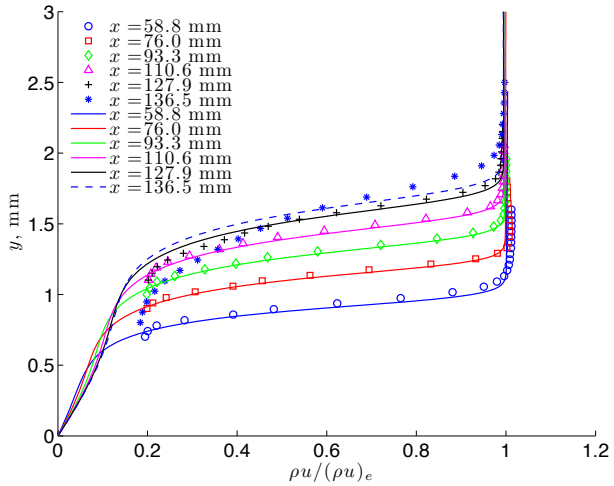

Figure 12: Comparison of the measured and computed mean mass-flux profiles along the roughness-wake centerline. The symbols in the plot denote experimental data and the lines in the plot denote the computational results. The nominal freestream conditions were $\mathbf{P_o} = 206.8$ kPa, $\mathbf{T_o} = 319.3$ K, and $\mathbf{Re} = 10.8 \times 10^6$ m^{-1}.

The measured and computed mean mass-flux contours in the y-z plane at two streamwise stations are shown in Fig. 11. For the first streamwise station of $x = 110.6$ mm, where the mean flow is laminar, the agreement between the measurements and computations is very good. The computations capture the upwelling of fluid on the roughness-wake centerline and they capture the formation of a high-speed streak at a spanwise location that is in close agreement with the measurements. As we move away from the centerline in the spanwise direction, the boundary layer approaches its undisturbed state. Here, the measured boundary layer is slightly thicker than the computed flow. This is consistent with our baseline measurements, which indicated a boundary layer thickness that was slightly larger than the theoretical similarity solution used for the computational inflow condition. For the second streamwise station of $x = 136.5$ mm, where the wake flow is in the beginning stages of breakdown, we observe clear quantitative differences between the computed laminar flow and the measurements, particularly in regions of high wall-normal and spanwise shear. Here, the Reynolds stresses associated with the transitional flow have reached a large enough level to modify the mean flow and this behavior is not, of course, captured by the laminar-flow computations.

The measured (symbols) and computed (lines) mean mass-flux profiles along the roughness-wake centerline are compared in Fig. 12. Here, the agreement is very good up to a streamwise location of $x = 110.6$ mm, where is the flow is still laminar. Beyond that point, the increased Reynolds stresses associated with the transitional flow cause progressively increasing deviations between the measured and computed mean flow. Nevertheless, in the laminar region of the flow, the overall agreement between the measured and computed mean flow is quite good, and that gives us confidence to proceed with the stability calculations.

5.0 CONCLUSIONS AND FUTURE WORK

In this paper, we have presented our progress on a joint experimental and numerical study of laminar-to-turbulent transition induced by an isolated roughness element in a high-speed laminar boundary layer. The numerical analysis suggests that transition is driven by the instability of high- and low-speed streaks embedded in the wake of the isolated roughness element. In addition, spatial stability analysis revealed that the wake flow supports multiple modes (even and odd) of convective instabilities that experience strong enough growth to cause transition. The experimental measurements, which included hot-wire and pitot-probe surveys, confirmed the existence of embedded high- and low-speed streaks in the roughness wake. Furthermore, the measurements indicate the presence of both even and odd modes of instability, although their relative magnitude depends on the specifics of the roughness and flow conditions (*e.g.*, the value of Re_{kk} or k/δ). For a test case with $Re_{kk} = 462$, the breakdown to turbulence appears to be driven by the even mode of instability. For a lower roughness Reynolds number of $Re_{kk} = 319$, however, the odd mode was found to be more dominant than the even mode and it is expected to play a more prominent role in the transition process for this case.

Mean-flow computations for a roughness case that matches the conditions of the experiment were performed and overall, they agree very well with the measurements. A stability analysis of this computed mean flow is currently underway. Forthcoming tunnel entries in the SLDT will examine parametric effects on transition. More specifically, we plan to consider different roughness heights, planform shapes, and aspect ratios in our measurement campaign.

REFERENCES

[1] McGinley, C. B., Berry, S. A., Kinder, G. R., Barnwell, M., Wang, K. C., and Kirk, B. S., "Review of Orbiter Flight Boundary Layer Transition Data," AIAA Paper 2006-2921, June 2006.

[2] Berry, S. A., Auslender, A. H., Dilley, A. D., and Calleja, J. F., "Hypersonic Boundary-Layer Trip Development for Hyper-X," *Journal of Spacecraft and Rockets*, Vol. 38, No. 6, November-December 2001, pp. 853–864.

[3] Reda, D. C., "Review and Synthesis of Roughness-Dominated Transition Correlations for Reentry Applications," *Journal of Spacecraft and Rockets*, Vol. 39, No. 2, March–April 2002, pp. 161–167.

[4] Choudhari, M., Li, F., Wu, M., Chang, C., Edwards, J., Kegerise, M., and King, R., "Laminar-Turbulent Transition behind Discrete Roughness Elements in a High-Speed Boundary Layer," AIAA Paper 2010-1575, January 2010.

[5] Beckwith, I. E., Creel, T. R., Chen, F.-J., and Kendall, J. M., "Free-Stream Noise and Transition Measurements on a Cone in a Mach 3.5 Pilot Low-Disturbance Tunnel," NASA TP 2180, September 1983.

[6] Chen, F.-J., "Boundary-Layer Transition Extent Measurements on a Cone and Flat Plate at Mach 3.5," AIAA Paper 93-0342, January 1993.

[7] Kegerise, M. A., Owens, L. R., and King, R. A., "High-Speed Boundary-Layer Transition Induced by an Isolated Roughness Element," AIAA Paper 2010-4999, June 2010.

[8] Smits, A. J., Hayakawa, K., and Muck, K. C., "Constant Temperature Hot-Wire Anemometer Practice in Supersonic Flows, Part 1: The Normal Wire," *Experiments in Fluids*, Vol. 1, 1983, pp. 83–92.

[9] Choi, J. I., Oberoi, R. C., Edwards, J. R., and Rosati, J. A., "An Immersed Boundary Method for Complex Incompressible Flows," *Journal of Computational Physics*, Vol. 224, 2007, pp. 757–784.

[10] Ghosh, S., Choi, J. I., and Edwards, J. R., "RANS and Hybrid LES/RANS Simulation of the Effects of Micro Vortex Generators using Immersed Boundary Methods," AIAA Paper 2008-3728, June 2008.

[11] Choudhari, M., Li, F., and Edwards, J. A., "Stability Analysis of Roughness Array Wake in a High-Speed Boundary Layer," AIAA Paper 2009-170, January 2009.

[12] Li, F. and Choudhari, M., "Spatially Developing Secondary Instabilities and Attachment Line Instability in Supersonic Boundary Layers," AIAA Paper 2008-590, January 2008.

[13] http://vulcan-cfd.larc.nasa.gov, November 2010.